Compact models for carrier-injection silicon microring modulators

Rui Wu,[1,2,*] **Chin-Hui Chen,**[2] **Jean-Marc Fedeli,**[3] **Maryse Fournier,**[3] **Kwang-Ting Cheng,**[1] **and Raymond G. Beausoleil**[2]

[1]*Department of Electrical & Computer Engineering, University of California, Santa Barbara, CA 93106, USA*
[2]*HP Labs, Hewlett-Packard Company, Palo Alto, CA 94304, USA*
[3]*CEA, LETI, Minatec Campus, 38054 Grenoble, France*
[*]*ruiwu@ece.ucsb.edu*

Abstract: We propose compact DC and small-signal models for carrier-injection microring modulators that accurately describe the DC characteristics (resonance wavelength, quality factor, and extinction ratio) and the high frequency performance. The proposed theoretical models provide physical insights of the carrier-injection microring modulators with a variety of designs. The DC and small-signal models are implemented in Verilog-A for SPICE-compatible simulations.

© 2015 Optical Society of America

OCIS codes: (250.7360) Waveguide modulators; (230.2090) Electro-optical devices; (230.3120) Integrated optics devices; (250.5300) Photonic integrated circuits; (200.4650) Optical interconnects;

References and links

1. R. G. Beausoleil, M. McLaren, and N. P. Jouppi, "Photonic architectures for high-performance data centers," IEEE J. Sel. Top. Quantum Electron. **19**, 3700109 (2013).
2. Q. Xu, S. Manipatruni, B. Schmidt, J. Shakya, and M. Lipson, "12.5 Gbit/s carrier-injection-based silicon micro-ring silicon modulators," Opt. Express **15**, 430–436 (2007).
3. S. Manipatruni, Q. Xu, B. Schmidt, J. Shakya, and M. Lipson, "High speed carrier injection 18 Gb/s silicon micro-ring electro-optic modulator," in "Lasers and Electro-Optics Society, 2007. The 20th Annual Meeting of the IEEE," (IEEE, 2007), pp. 537–538.
4. T. Baba, S. Akiyama, M. Imai, N. Hirayama, H. Takahashi, Y. Noguchi, T. Horikawa, and T. Usuki, "50-Gb/s ring-resonator-based silicon modulator," Opt. Express **21**, 11869–11876 (2013).
5. C. Li, C. Chen, B. Wang, S. Palermo, M. Fiorentino, and R. Beausoleil, "An energy-efficient silicon microring resonator-based photonic transmitter," IEEE Design Test **31**, 46–54 (2014).
6. X. Zheng, J. Lexau, Y. Luo, H. Thacker, T. Pinguet, A. Mekis, G. Li, J. Shi, P. Amberg, N. Pinckney, K. Raj, R. Ho, J. E. Cunningham, and A. V. Krishnamoorthy, "Ultra-low-energy all-cmos modulator integrated with driver," Opt. Express **18**, 3059–3070 (2010).
7. G. Li, X. Zheng, J. Yao, H. Thacker, I. Shubin, Y. Luo, K. Raj, J. E. Cunningham, and A. V. Krishnamoorthy, "25Gb/s 1V-driving CMOS ring modulator with integrated thermal tuning," Opt. Express **19**, 20435–20443 (2011).
8. P. Dong, S. Liao, D. Feng, H. Liang, D. Zheng, R. Shafiiha, C.-C. Kung, W. Qian, G. Li, X. Zheng, A. V. Krishnamoorthy, and M. Asghari, "Low Vpp, ultralow-energy, compact, high-speed silicon electro-optic modulator," Opt. Express **17**, 22484–22490 (2009).
9. K. Zhu, V. Saxena, and W. Kuang, "Compact verilog-A modeling of silicon traveling-wave modulator for hybrid cmos photonic circuit design," in "2014 IEEE 57th International Midwest Symposium on Circuits and Systems (MWSCAS)," (IEEE, 2014), pp. 615–618.
10. M. De Wilde, O. Rits, R. Bockstaele, J. M. Van Campenhout, and R. G. Baets, "Circuit-level simulation approach to analyze system-level behavior of VCSEL-based optical interconnects," in "Photonics Fabrication Europe," (ISOP, 2003), pp. 247–257.
11. P. Martin, F. Gays, E. Grellier, A. Myko, and S. Menezo, "Modeling of silicon photonics devices with verilog-A," in "2014 29th International Conference on Microelectronics Proceedings," (MIEL, 2014), pp. 209–212.

#235435 - $15.00 USD Received 26 Mar 2015; accepted 28 May 2015; published 4 Jun 2015
(C) 2015 OSA

12. Lumerical, "Lumerical interconnect product overview," https://www.lumerical.com/tcad-products/interconnect/.
13. RSoft, "Optsim circuit product overview," http://optics.synopsys.com/rsoft/rsoft-optsim-circuit.html.
14. C. Sun, C.-H. Chen, G. Kurian, L. Wei, J. Miller, A. Agarwal, L.-S. Peh, and V. Stojanovic, "DSENT: a tool connecting emerging photonics with electronics for opto-electronic networks-on-chip modeling," in "IEEE/ACM International Symposium on Networks on Chip (NoCS)," (IEEE, 2012), pp. 201–210.
15. W. D. Sacher and J. K. Poon, "Dynamics of microring resonator modulators," Opt. Express **16**, 15741–15753 (2008).
16. Z. Peng, D. Fattal, M. Fiorentino, and R. Beausoleil, "Fabrication variations in soi microrings for dwdm networks," in "2010 7th IEEE International Conference on Group IV Photonics (GFP)," (IEEE, 2010), pp. 120–122.
17. R. A. Soref and B. R. Bennett, "Electrooptical effects in silicon," Quantum Electronics, IEEE Journal of **23**, 123–129 (1987).
18. J. Bovington, R. Wu, K.-T. Cheng, and J. E. Bowers, "Thermal stress implications in athermal TiO2 waveguides on a silicon substrate," Opt. Express **22**, 661–666 (2014).
19. T. Visser, H. Blok, B. Demeulenaere, and D. Lenstra, "Confinement factors and gain in optical amplifiers," Quantum Electronics, IEEE Journal of **33**, 1763–1766 (1997).
20. G. T. Reed and A. P. Knights, *Silicon Photonics: An Introduction* (John Wiley & Sons, 2004).
21. S. Manipatruni, K. Preston, L. Chen, and M. Lipson, "Ultra-low voltage, ultra-small mode volume silicon microring modulator," Opt. Express **18**, 18235–18242 (2010).
22. Z. Peng, D. Fattal, M. Fiorentino, and R. Beausoleil, "CMOS-compatible microring modulators for nanophotonic interconnect," in "Integrated Photonics Research, Silicon and Nanophotonics and Photonics in Switching" (OSA, 2010).
23. A. Yariv, "Universal relations for coupling of optical power between microresonators and dielectric waveguides," Electron. Lett. **36**, 321–322 (2000).

1. Introduction

Silicon photonics recently become the focal point for high-performance computing and interconnects [1]. Microring modulators are important devices in silicon photonic interconnects, among which the carrier-injection p-i-n type and the carrier-depletion p-n type are widely reported [2–8]. The carrier-depletion type has a high intrinsic bandwidth, as it does not rely on slow diffusion of minority carriers [6, 7]. However, the carrier-injection type outperforms the carrier-depletion one in modulation depth and insertion loss due to the large change of refractive index [2, 8]. Meanwhile, the speed of the carrier-injection microring modulator can be greatly enhanced by a pre-emphasis driving scheme [2–5].

Integrating silicon photonic devices into modern CMOS-VLSI design flows requires co-design of electronic and photonic integrated circuits, in which compact models for nanophotonic devices are needed. Researchers have proposed Verilog-A compact models for the Mach-Zehnder modulator [9], the VCSEL [10], and the pulsed optical source and the photodetector [11]. The carrier-depletion microring modulator has also been compactly modeled in many photonic link simulators (e.g., Lumerical Interconnect [12], RSoft OptSim Circuit [13], and DSENT [14]). Sacher et al. proposed a dynamic model for microring modulators in [15]. However, the characteristics of the carrier-injection microring modulator, e.g., the resonance wavelength shift with respect to bias conditions, have not been accurately modeled. In this paper, we develop compact DC and small-signal models for carrier-injection modulators to provide physical insights to the device performance for a variety of designs.

The resonance wavelength shift in the microring modulator is essential for the on-off keying modulation. Therefore, we derive a theoretical equation for the resonance wavelength shift. The equation is capable of distinguishing the electro-optical blueshift effect and the thermo-optic redshift effect, enabling the analysis of the device design parameters' impact on the modulator's DC performance. Additionally, the quality factor $\mathbb{Q}$ and the extinction ratio ER are important to determine the link power budget and signal quality [16]. Meanwhile, the $\mathbb{Q}$ and the ER of the carrier-injection microring modulator change significantly with injected current. Therefore, we quantify the dependence of the $\mathbb{Q}$ and the ER on the injected current.

In order to characterize the high-speed behavior of the carrier-injection microring modulator,

#235435 - $15.00 USD Received 26 Mar 2015; accepted 28 May 2015; published 4 Jun 2015
(C) 2015 OSA

we propose a small-signal circuit model. The small-signal circuit parameters are extracted from S11 measurements. The small-signal circuit matches the device structure and provides insights to the dependence of small-signal capacitances and resistances on bias points and design parameters. The small-signal model, together with the DC spectrum model, is implemented in Verilog-A to facilitate co-simulations of photonic and electronic circuits.

2. Device designs and fabrications

Figure 1(a) shows a microscopic image of a microring modulator fabricated in CEA-LETI's silicon photonic SOI process. The rib section of the microring waveguide is 250 nm x 450 nm, and a slab section of 50 nm is used to inject carriers from the p-doped (3×10^{19}cm^{-3}) and n-doped (3×10^{19}cm^{-3}) regions, as shown in the Fig. 1(b) inset. There are several device design variants including microring diameter, guard distance (GD) between the boundary of doped region and rib waveguide, and the coupling gap between the ring waveguide and the bus waveguide. As part of process development, 25 wafers are used for engineering purposes. A set of short-loop wafers (Batch B) are processed through some subset of the total process steps to provide a snapshot of process reliability and modulators performance before the final delivery. We find that the contact resistance in this batch is significantly higher than the expected value due to miscalculation of the via etch depth. This contact resistance error has been corrected in the final delivery (Batch A).

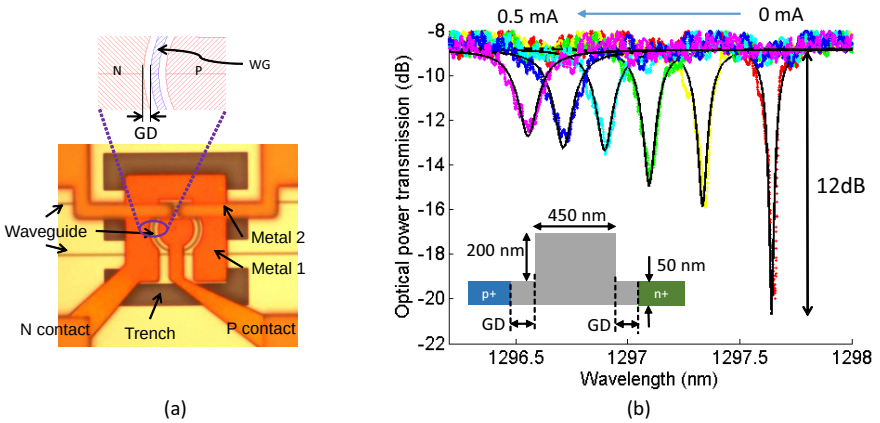

Fig. 1. (a) A microscopic image of a microring modulator with 10 μm diameter; (b) Transmission spectra sequence with bias current ranging from 0 to 0.5 mA; the colorful dots: measurement, the black lines: model; the inset shows the cross section of the microring waveguide.

In the experimental setup, vertical fiber-to-chip grating couplers are used to provide optical input and output access. Using a tunable laser, a DC voltage source, and an optical power meter, we measure the transmission spectra sequence of a microring modulator with different bias current, as shown in Fig. 1(b). The microring modulator has a quality factor of 12,000 at zero injection, and achieves an on/off extinction ratio of 12 dB.

3. Electro-optic modulation models

The electro-optic modulation of microring resonators utilizes the plasma dispersion effect, in which the refractive index and optical loss of silicon are altered by changing the carrier concentration [17]. As the silicon index changes, the resonance wavelength shifts. Meanwhile, the

#235435 - $15.00 USD Received 26 Mar 2015; accepted 28 May 2015; published 4 Jun 2015
(C) 2015 OSA

quality factor and extinction ratio also change due to the increase of the optical loss. We derive theoretical models for the resonance wavelength, the extinction ratio, and the quality factor.

3.1. Resonance wavelength shift

The electro-optic (EO) effect changes the silicon refractive index, the mode effective index, and in turn the resonance wavelength. The relationship between the EO effect induced resonance wavelength shift $\Delta\lambda_r^{EO}$ and the carrier concentration change ΔN is given by:

$$\Delta\lambda_r^{EO} = -\frac{\lambda_r}{n_g}\Gamma n_f \Delta N \tag{1}$$

where n_g is the group index of the optical mode; Γ is the mode confinement factor [18, 19]; $n_f \approx 2.13\times10^{-21}\text{cm}^3$ is the ratio between the change of silicon index and the change of carrier concentration when $\Delta N \sim 10^{18}\text{cm}^{-3}$ [2, 17, 20].

The steady state injected charge Q_{inj} in the p-i-n junction can be described by the following nonlinear equation [21]:

$$Q_{inj} = I\tau_c = I\frac{\tau_0}{1+Q_{inj}/Q_0} \Rightarrow Q_{inj} = \frac{Q_0}{2}\left(\sqrt{1+\frac{4I\tau_0}{Q_0}}-1\right) \tag{2}$$

where τ_0 is the carrier lifetime at a low carrier density; Q_0 is a fitting parameter describing the dependence of carrier lifetime on the carrier density [21]. Considering the carrier concentration change $\Delta N = Q_{inj}/q\mathbb{V}$ where $\mathbb{V}$ is the junction volume, we can derive the lumped equation for the EO effect induced resonance wavelength shift:

$$\Delta\lambda_r^{EO} = -\frac{\lambda_r\Gamma}{n_g}n_f\frac{Q_0}{2q\mathbb{V}}\left(\sqrt{1+\frac{4I\tau_0}{Q_0}}-1\right) \triangleq -a\cdot(\sqrt{1+I/I_0}-1) \tag{3}$$

In a practical carrier-injection modulator, the thermo-optic (TO) effect caused by the self-heating of the injected current is non-negligible. The silicon index increases with the temperature:

$$\Delta n_{Si} = \frac{\mathrm{d}n_{Si}}{\mathrm{d}T}\cdot\Delta T \tag{4}$$

The temperature rise ΔT can be characterized as $\Delta T = \theta I^2 R$, where θ is the thermal impedance of the p-i-n junction. Therefore, the TO effect induced resonance wavelength shift is:

$$\Delta\lambda_r^{TO} = \frac{\lambda_r\Gamma}{n_g}\frac{\mathrm{d}n_{Si}}{\mathrm{d}T}\theta R\cdot I^2 \triangleq c\cdot I^2 \tag{5}$$

Consequently, the total resonance wavelength shift is given by:

$$\Delta\lambda_r^{total} = \Delta\lambda_r^{EO} + \Delta\lambda_r^{TO} = -a\cdot(\sqrt{1+I/I_0}-1) + c\cdot I^2 \tag{6}$$

The $\Delta\lambda_r$ model in Eq. (6) results in excellent fitting with the measured data from different device designs and fabrication batches, as shown in Figs. 2 and 3. It should be noted that though the injection current in the testing experiments goes up to 3 or 4 mA, the actual bias of the device is usually limited in order to avoid the excess $I\cdot V$ power consumption and severe degradation of $\mathbb{Q}$ and ER. For comparison, the measured $\Delta\lambda_r$ is also fitted using the empirical polynomial model ($\Delta\lambda_r = -a\cdot I + b\cdot I^2$) in [22]. The fitting results demonstrate that the maximum fitting errors using our proposed model are only about 10% for Batch A and about 20% for Batch B of those using the polynomial model. Overall, our model provides a much better fitting accuracy

#235435 - $15.00 USD Received 26 Mar 2015; accepted 28 May 2015; published 4 Jun 2015
(C) 2015 OSA

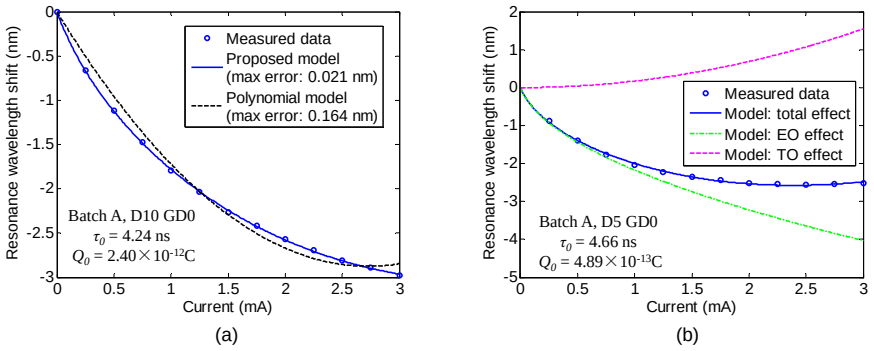

Fig. 2. (a) Measured resonance wavelength shift with fitting results using our proposed model and empirical polynomial model; (b) Decomposition of wavelength shift to eletro-optic and thermo-optic effect.

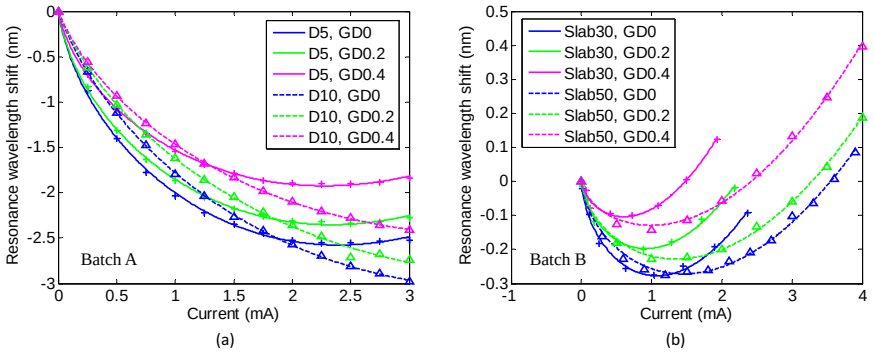

Fig. 3. Resonance wavelength shift of modulators with model fitting: (a) Batch A with different diameters (D in μm) and guard distances (GD in μm); (b) Batch B with different slab heights (in nm) and GDs. (Symbols: measured data, line: model fitting)

than the polynomial model, since out model captures the nonlinear dependence of the EO effect on the injected current.

Our model can decompose $\Delta\lambda_r$ to electro-optic (EO) effect and thermo-optic (TO) effect separately as shown in Fig. 2 (b). The EO and TO effect coefficients summarized in Fig. 4 have several implications on the device design parameters: First, the modulators with a 5 μm diameter have a slightly smaller EO effect than that of 10 μm diameter in terms of the metric $a/\sqrt{I_0}$, while D5's TO effect (in terms of c) is about twice as that of D10. Second, for all devices, as the guard distance increases, the EO effect decreases while the TO effect fluctuates irregularly. Third, the devices with a 30 nm slab height have slightly greater EO effect and about two times TO effect than those of a 50 nm slab height. Fourth, by comparing the modulators with a 10 μm diameter and a 50 nm slab height from Batches A and B, one can see that Batch A's EO effect is much greater than that of Batch B, because the process error has been corrected in Batch A and the injection efficiency is greatly improved.

#235435 - $15.00 USD Received 26 Mar 2015; accepted 28 May 2015; published 4 Jun 2015
(C) 2015 OSA

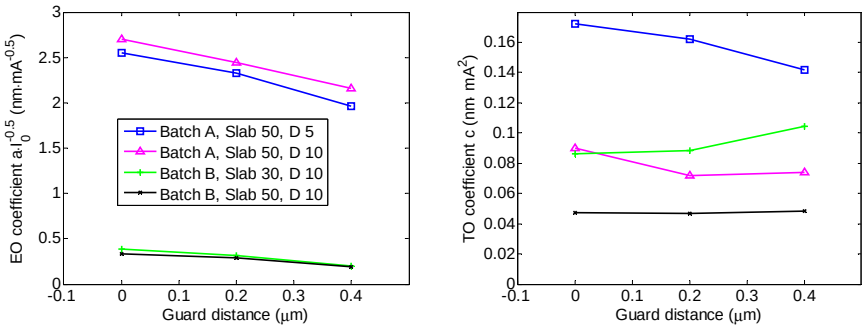

Fig. 4. Fitting results of the resonance wavelength model for devices with different fabrications, diameters (D), and slab heights: (a) EO effect (metric: $a/\sqrt{I_0}$); (b) TO effect (metric: c).

3.2. *Change of extinction ratio and quality factor*

When carriers are injected into a microring modulator, ER and $\mathbb{Q}$ change since the optical loss within the microring increases. The dependence of ER and $\mathbb{Q}$ on the intra-microring optical field loss coefficient α can be derived from Yariv's transmission relation in [23]:

$$T(\lambda) = 1 - \frac{(1-t^2)(1-e^{-2\alpha l})}{(1-te^{-\alpha l})^2 + (2t^{1/2}e^{-\alpha l/2}\sin(\pi n_{eff} l/\lambda))^2} \tag{7}$$

where t is the through-coupling coefficient that is related to the cross-coupling coefficient κ by $t^2+\kappa^2=1$; l is the microring circumference. The transmission spectrum around a resonance wavelength ($\lambda_r = n_{eff} l/m$) can be approximated by:

$$T(\Delta\lambda) = 1 - \frac{A}{1+(2\mathbb{Q}\cdot\Delta\lambda/\lambda_r)^2} \tag{8}$$

with

$$A = 1 - \left(\frac{t-e^{-\alpha l}}{1-te^{-\alpha l}}\right)^2, \quad \mathbb{Q} = m\pi\frac{t^{1/2}e^{-\alpha l/2}}{1-te^{-\alpha l}} \tag{9}$$

where A is related to ER by $ER = 1/(1-A)$. The loss coefficient α increases with the increase of the carrier concentration:

$$\alpha = \alpha_0 + n_a\Delta N = \alpha_0 + n_a\frac{Q_0}{2q\mathbb{V}}\left(\sqrt{1+\frac{4I\tau_0}{Q_0}}-1\right) \tag{10}$$

By incorporating Eq. (10) into Eq. (9), we can obtain the models for ER and $\mathbb{Q}$ as functions of the injected current I.

The effectiveness of the models is demonstrated by three devices with different coupling gaps on three coupling conditions, as shown in Fig. 5. In the over coupled case, the fitting parameter $t < \exp(-\alpha_0 l)$. As the injected current and thus optical loss increases, the $\exp(-\alpha l)$ decreases to be equal to t and then smaller than t. As a result, the ER (or A) first increases to reach infinity (or unity) from over coupled to critical coupled, and then decreases into the under coupled regime. Our model is consistent with the non-monotonic change of ER. In the over coupled case, the relatively large discrepancy between the model and the measurement may be due to the abrupt change of ER around the critical coupled condition. In the critical coupled (or under coupled) case, our model shows both good fitting results as well as reasonable fitting parameters with t equals to (or greater than) $\exp(-\alpha_0 l)$.

#235435 - $15.00 USD Received 26 Mar 2015; accepted 28 May 2015; published 4 Jun 2015
(C) 2015 OSA

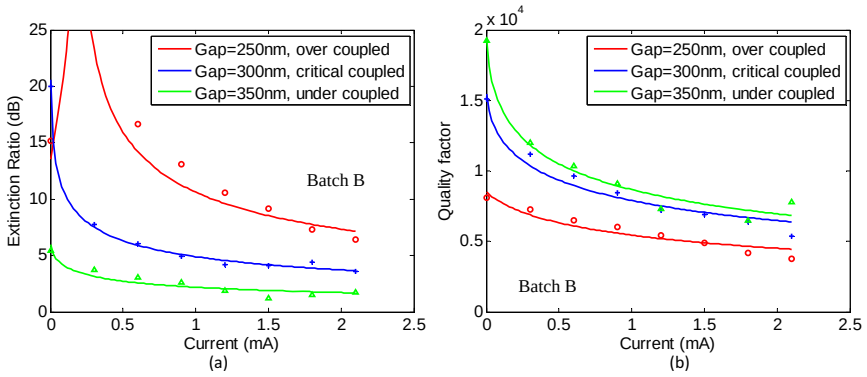

Fig. 5. Measured data (circles) and model fitting results (lines) for (a) extinction ratio and (b) quality factor of devices with different coupling gaps and coupling cases. The devices are from Batch B with a 5 μm diameter, a 0.4 μm guard distance, and a 50 nm slab height.

4. Electrical models

4.1. *DC model*

The governing equation describing the static I-V characteristics of the carrier-injection modulator is given by [21]:

$$I = I_S \exp\{q(V - IR - V_t)/(nkT)\} \tag{11}$$

where I_S is the reverse saturation current; R is the total series resistance including p/n doped region resistance, interconnect resistance and DC probe contact resistance during testing; n is the ideality factor. As illustrated in Fig. 6, the model shows that the devices with a diameter of 5 and 10 μm (denoted as D5 and D10) have similar V_t and n, while the resistance of D5 is almost twice of that of D10 because the microring circumference of D5 is half of that of D10.

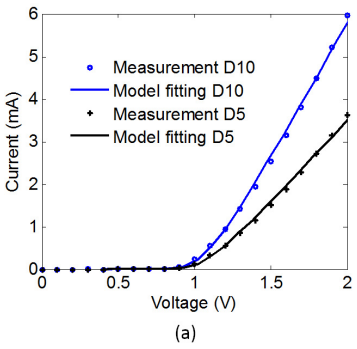

Ring diameter (μm)	V_t (V)	R (Ω)	I_S (nA)	n
10	0.427	147.0	2.196	1.905
5	0.403	240.3	1.000	1.956

(b)

Fig. 6. Measured and model fitted I-V curves of modulators with different diameters.

4.2. *Small-signal circuit model*

In order to better understand the high speed performance of the carrier-injection modulator, we develop a small-signal circuit model with physical origins as shown in Figs. 7(a) and 7(b). In the small-signal circuit, C_D and R_D respectively model the capacitance and resistance in the forward-biased p-i-n diode junction; C_{OX} denotes the capacitance through the cladding and

#235435 - $15.00 USD Received 26 Mar 2015; accepted 28 May 2015; published 4 Jun 2015
(C) 2015 OSA

buried SiO_2 layers; R_{s1} and R_{s2} model the resistances of doped silicon; C_p represents the capacitance between the electrodes. The small-signal circuit parameters are extracted by measuring and curve-fitting the S11 test data. The Figs. 7(c) and 7(d) demonstrates the good curve-fitting results using the small-signal circuit model.

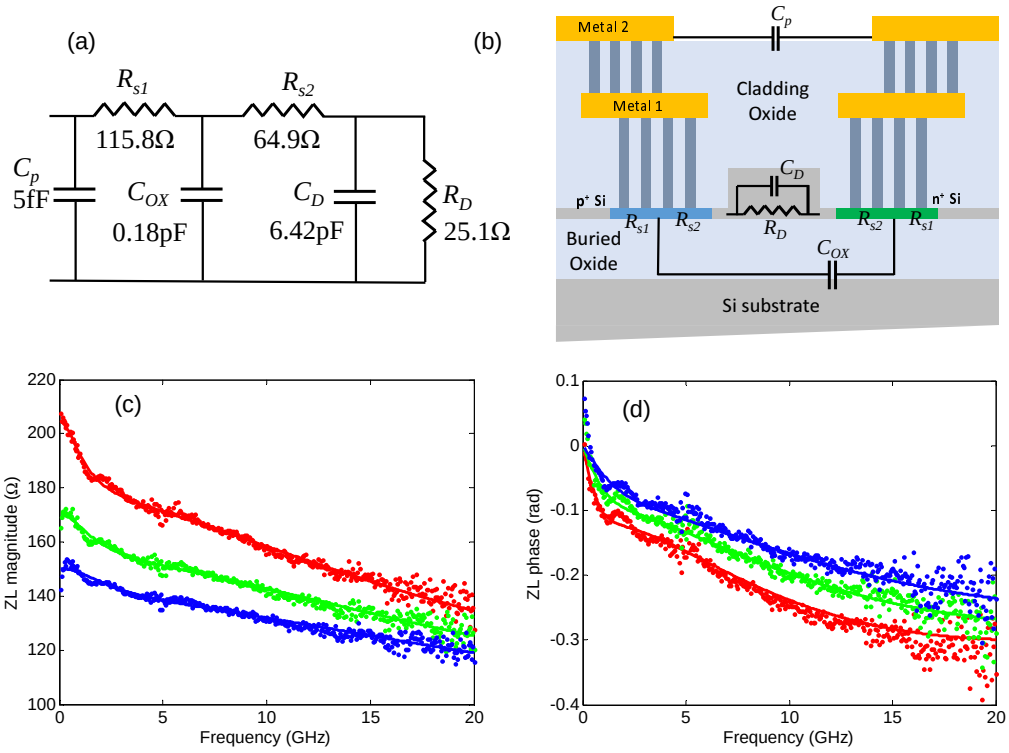

Fig. 7. (a) The small-signal circuit model with circuit values at 1mA bias points; (b) The cross-section of the microring waveguide; (c)(d) Curve-fitting of the measured load impedance Z_L of the modulator with a 10 μm diameter. (bias points: red 1 mA, green 2 mA, blue 3 mA)

Using the small-signal circuit model, we estimate the RC-limited 3dB frequencies for devices with different diameters and injection levels (Fig. 8). The equation for the RC-limited 3dB frequency is $1/(2\pi((R_{s1}+R_{s2})//R_D)C_D)$, based on the approximation that both C_p and C_{OX} are much smaller than C_D. From Fig. 8, one can see that the RC-limited device bandwidth increases with the increasing of the injection level. The Fig. 8 also demonstrates that the device with a 5μm diameter has a higher RC-limited bandwidth than that of 10 μm. It should be noted that though the carrier-injection modulator inherently has a low electrical bandwidth limit, the optical modulation speed can be greatly improved by using pre-emphasis schemes [2–5].

5. Model implementations in Verilog-A

The proposed DC and small-signal models have been implemented in Verilog-A. We use electrical voltage to mimic optical power, so that our Verilog-A models are compatible with common SPICE simulators. In the DC Verilog-A model, the optical output power is implemented as a function of the optical input power, the model parameters A, $\mathbb{Q}$ and λ_r, and the injected current. In the small-signal Verilog-A model, the small-signal circuit is represented by a RC network,

#235435 - $15.00 USD Received 26 Mar 2015; accepted 28 May 2015; published 4 Jun 2015
(C) 2015 OSA

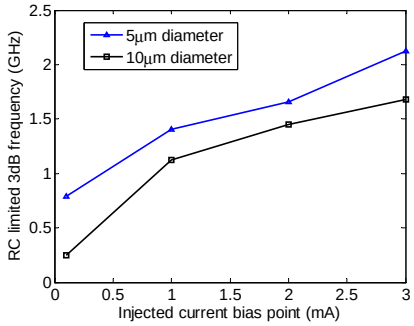

Fig. 8. The RC limited 3dB frequency predicted by the small-signal circuit model for devices with diameter of 5 μm and 10 μm at different bias points. The minimum bias point is 0.1 mA instead of 0 mA because the p-i-n junction needs a positive bias to be turned on for small-signal modulation. The guard distance of the microring modulator is 0.

where the current through R_D is the injected current I in the transmission spectrum model in the Section 3.

Our Verilog-A models can be used in the Synopsys HSPICE environment. Since it would be insightful to observe the device's characteristics with respect to applied voltages, we simulate the optical transmission versus applied voltage curves for a variety of operating wavelengths as shown in Fig. 9(a). One can see that as the operating wavelength deviates from the microring resonance wavelength, the optimal DC operating points (shown as black dots) varies. The maximum achievable extinction ratio also decreases as the operating wavelength deviates, because our DC models capture the dependence of ER on the injected current. Our small-signal model is used in the electro-optic AC simulations as shown in Fig. 9(b). The AC simulation results show that greater bias leads to a higher bandwidth, which agrees with the trend in Fig. 8.

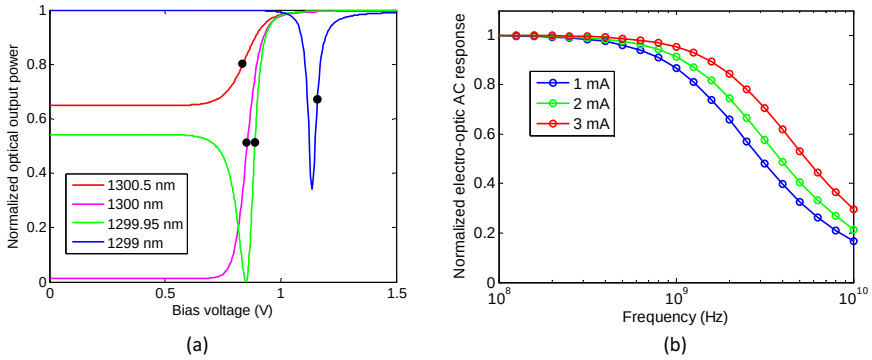

Fig. 9. (a) DC simulations of the modulator model for different operating wavelengths; the microring resonance wavelength at zero bias is 1300 nm; the black dots represent the optimal DC operating points for different wavelengths. (b) Electro-optic AC simulations of a microring modulator.

#235435 - $15.00 USD Received 26 Mar 2015; accepted 28 May 2015; published 4 Jun 2015
(C) 2015 OSA

6. Conclusion

In this paper, we present theoretical DC models for carrier-injection microring modulators to characterize the resonance wavelength, quality factor, and extinction ratio with respect to the injected current. A small-signal circuit model is also proposed to characterize the high-speed performance of carrier-injection microring modulators. This set of models provides valuable physical insights to the device performance for a variety of designs and fabrication batches. We implement the proposed models in Verilog-A, which facilitates the SPICE-compatible co-simulation of electronic and photonic circuits.

Acknowledgments

The authors would like to thank Dr. Wayne Sorin and Dr. Tsung-Ching Huang from HP Labs, and Prof. John Bowers and Chong Zhang from UCSB for their helpful advises. R. Wu and K.-T. Cheng acknowledge the Semiconductor Research Corporation for the support.